Diverse magnetic phase diagram and anomalous Hall effect in antiferromagnetic $LuMn_6Sn_6$

Shirin Mozaffari,[1,*,†] Seung-Hwan Do,[1] Richa P. Madhogaria,[1] Aikaterini Flessa Savvidou,[2,3] Brian W. Casas,[2] William R. Meier,[1] Rui Xue,[4] Eun Sang Choi,[2,3] Luis Balicas,[2,3] and David G. Mandrus[1,5,‡]

[1]*Department of Materials Science and Engineering, The University of Tennessee, Knoxville, Tennessee 37996, USA*
[2]*National High Magnetic Field Laboratory, Florida State University, Tallahassee, Florida 32310, USA*
[3]*Department of Physics, Florida State University, Tallahassee, Florida 32306, USA*
[4]*Department of Physics and Astronomy, The University of Tennessee, Knoxville, Tennessee 37996, USA*
[5]*Materials Science and Technology Division, Oak Ridge National Laboratory, Oak Ridge, Tennessee 37831, USA*

(Received 27 April 2025; revised 28 June 2025; accepted 25 August 2025; published 26 September 2025)

The interactions between conduction electrons and magnetism can significantly enhance the Hall signal, a phenomenon known as the anomalous Hall effect (AHE). While the AHE is generally not expected in antiferromagnets, a large AHE is observed in certain antiferromagnets with noncollinear spin textures and nonvanishing Berry curvature. In this work, we present a rich temperature and magnetic phase diagram with eight distinct magnetic phases for the antiferromagnetic kagome compound $LuMn_6Sn_6$. The Hall effect analysis in $LuMn_6Sn_6$ reveals both intriguing physical phenomena and methodological challenges. In the coplanar canted antiferromagnetic phase, we observe an AHE, which likely originates from the intrinsic effects. At low temperatures, upon entering the ferromagnetic phase, the AHE sharply increases and exceeds the conventional limits expected from intrinsic mechanisms. We also demonstrate the limitations of standard experimental methods in extracting the topological contribution to the Hall effect data. In particular, we show that accounting for magnetoresistance anisotropy helps reduce spurious contribution that can mimic topological Hall signals, although it does not fully resolve it. These shortcomings in current approaches in partitioning the Hall response necessitate new tools to interpret transport results in complex magnetic materials such as $LuMn_6Sn_6$.

DOI: 10.1103/hwz4-z9mm

I. INTRODUCTION

The electrical Hall effect serves as a widely used probe to explore topological effects in magnetic systems. The Hall current requires breaking time-reversal symmetry. When this symmetry is broken by an external magnetic field, it results in the ordinary Hall effect. Alternatively, the magnetic field can induce internal magnetization, resulting in an additional contribution to the Hall current, referred to as the anomalous Hall effect (AHE) [1,2]. Intrinsic contributions to the AHE originate from the Berry curvature of the Bloch wave function, summed over all occupied states, analogous to the mechanism of the quantum Hall effect.

In ferromagnets with spontaneous magnetization, AHE can arise without the presence of an external magnetic field. Traditionally, the Hall effect has not been associated with antiferromagnetic (AF) order. However, recent theoretical and experimental studies have revealed significant Hall effects in certain magnetic crystals lacking global magnetization. Examples include the observation of a Hall effect in a spin-liquid candidate $Pr_2Ir_2O_7$ [3], certain noncollinear AF compounds such as Mn_3Sn, Mn_3Ge, MnGe, NbMnP, and Ce_2CuGe_6 [4–8], and the newly discovered Hall effect in altermagnetic materials [9]. Remarkably, the AHE in some of these antiferromagnets is comparable in strength to that observed in ferromagnets.

These discoveries led us to move away from viewing the Hall effect solely as arising from conventional symmetry-breaking processes. Instead, the Hall response is now understood to be closely tied to nontrivial topology in the electronic structure, resulting in an enhanced response that challenges the traditional paradigm of scaling with total magnetization strength [2].

In addition to the ordinary and anomalous Hall effects, noncoplanar spin alignments in real space can give rise to a finite scalar spin chirality, $\chi_{ijk} \sim s_i \cdot (s_j \times s_k)$, where $s_{i,j,k}$ are the spin moments of neighboring sites. This spin chirality can act as a local emergent magnetic field for conduction electrons, leading to a transverse response, termed the topological Hall effect (THE) [10–14].

Among the numerous compounds with magnetic topological behavior, the family of kagome structure materials is a quintessential embodiment of the concept. Examples include Fe_3Sn_2 [15,16], Fe_3Sn [17], Mn_3X (X = Sn, Ge, Pt, Rh, Ir) [4,18,19], $Co_3Sn_2S_2$ [20], and the family of RMn_6Sn_6 (R = Rare earth) [21]. The latter family, which is strongly frustrated, is the focus of this paper.

RMn_6Sn_6 family materials consists of kagome bilayers of Mn atoms that are separated by Sn and R atoms along the c axis. The family shows a collinear ferrimagnetic ground state with magnetic rare earths R = Gd–Er due to the strong AF coupling between R and Mn atoms [25–32]. The nonmagnetic rare earth analogues, R = Sc, Y, Lu, are antiferromagnets and consist of ferromagnetic (FM) double layers of the

*Contact author: shirinm@clemson.edu
†Present address: Department of Physics and Astronomy, Clemson University, Clemson, South Carolina 29634, United States.
‡Contact author: dmandrus@utk.edu

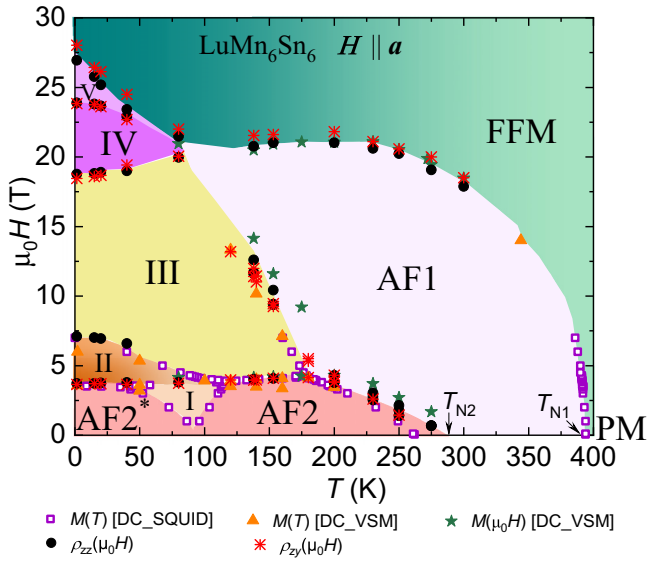

FIG. 1. Temperature (T) and magnetic field ($\mu_0 H$) phase diagram of $LuMn_6Sn_6$ for field applied along the crystallographic a axis. A variety of field-driven magnetic states are observed, including a collinear antiferromagnetic (AF1) and a forced ferromagnetic (FFM) phases. Under applied field, AF1 adopts a canted antiferromagnetic structure. Both AF2 and AF2* have a double spiral (DS) incommensurate structure, but with different periodicity [22]. Phases I and II show a commensurate antiferromagnetic order; Phase III adopts a transverse conical spiral (TCS) structure [22]. Comparison with the phase diagram of YMn_6Sn_6 [23,24] suggests that phase IV corresponds to a fan-like (FL) structure. The (H, T) phase diagram was constructed using DC magnetization (M), longitudinal (ρ_{zz}) and Hall resistivity (ρ_{zy}) measurements.

Mn kagome plane, which antiferromagnetically couple with neighboring bilayers [33–35].

RMn_6Sn_6 is reported to have several field-induced magnetic phases, and the observation of THE in one of these phases in R = Y, Sc, Er is among the most exciting phenomena reported for this family [28,36–38]. Beyond THE, RMn_6Sn_6 compounds have demonstrated other intriguing phenomena, including magnetization-driven Lifshitz transitions [24], a large anomalous transverse thermoelectric effect [39], and topological Nernst and thermal Hall effects [40,41]. Among the members of RMn_6Sn_6, $LuMn_6Sn_6$ is studied the least likely because of the very strong field required to induce the fully polarized state.

In this study, we delineate a rich field-temperature phase diagram for $LuMn_6Sn_6$ under a magnetic field applied along the crystalline a axis, as shown in Fig. 1. Such a rich phase diagram is rare and indicates the competition between multiple interactions. We identified eight different magnetic phases as a result of competition between FM and AF coupling between Mn kagome layers. To label the numerous magnetic phases, Roman numerals are used throughout this paper.

In addition to the diverse magnetic phase diagram, our Hall effect measurements shows an enhancement of an AHE contribution across the AF2–AF1 transition and at the boundary between phase IV (V) and the FFM state. Moreover, our study advocates for theoretical models over empirical relations and underscores the importance of considering magnetoresistance anisotropy in the analysis of nontrivial Hall responses. $LuMn_6Sn_6$ is ordered magnetically at room temperature and thus potentially has a direct application in the design of complex magnets for data storage.

II. EXPERIMENTAL DETAILS

Crystals of $LuMn_6Sn_6$ were grown from a tin flux using an atomic ratio of Lu:Mn:Sn = 1:6:30. The Lu pieces (Alfa Aesar 99.9%), Mn pieces (Alfa Aesar 99.95%), and Sn shot (Alfa Aesar 99.9999%) were loaded into an alumina crucible. The crucible assembly was sealed in a fused silica ampule and heated to 973°C over 12 h, then held for 12 h. The mixture was then cooled to 923°C at a rate of 2.5°C/h, followed by heating to 963°C over 2 h. Finally, it was cooled to 600°C at a rate of 1.5°C/h. At this temperature, the flux was separated from the crystals by inverting the tube and centrifuging. This process yielded blocky hexagonal crystals up to 1 cm in size [Fig. 2(a)]. The additional heating step to 963°C was included to promote the growth of larger crystals.

Powder x-ray diffraction measurement was performed using a Cu K_α x-ray source. Rietveld refinements confirms the $P6/mmm$ $HfFe_6Ge_6$-type structure of the sample (see Fig. S1 in the Supplemental Material (SM) [42]). Conventional magnetotransport experiments were performed in a physical property measurement system (PPMS-Quantum Design) under magnetic fields up to 14 T and temperatures as low as 1.8 K. Magnetization measurements under fields up to 7 T were performed in a commercial superconducting quantum interference device magnetometer (SQUID-Quantum Design). The high field magnetization and magnetotransport measurements were performed in a resistive Bitter magnet at the National High Magnetic Field Laboratory (NHMFL) in Tallahassee, FL, under continuous fields up to 35 T. A vibrating sample magnetometer (VSM) was used to measure DC magnetization. The measured longitudinal and transverse resistivities were field-symmetrized and antisymmetrized, respectively, to correct the effect of contact misalignment.

III. RESULTS AND DISCUSSION

A. Crystal structure analysis

$LuMn_6Sn_6$ has a hexagonal structure with space group $P6/mmm$ (No. 191), as shown in Fig. 2(b). The structure can be viewed as stacking layers of Lu, Mn, and Sn. Within each unit cell there are three different Sn sites (Sn1, Sn2, and Sn3) and two kagome planes of Mn atoms which are separated by different layers of LuSn3 and Sn1-Sn2-Sn1. Only Mn atoms possess magnetic moments which are aligned ferromagnetically within the ab-planes of the hexagonal lattice; the average of which in each Mn layer is shown schematically with an orange arrow in Fig. 2(c). Neutron diffraction in zero external magnetic field shows that the Mn layers across the Sn1-Sn2-Sn1 layers are coupled ferromagnetically but the coupling through the Lu-Sn3 layer is antiferromagnetic [33,34], as depicted in Fig. 2(c). This makes the magnetic unit cell in the AF1 phase twice the size of the chemical unit cell. The general magnetic structure in the RMn_6Sn_6 (R = Sc, Lu, Y) family

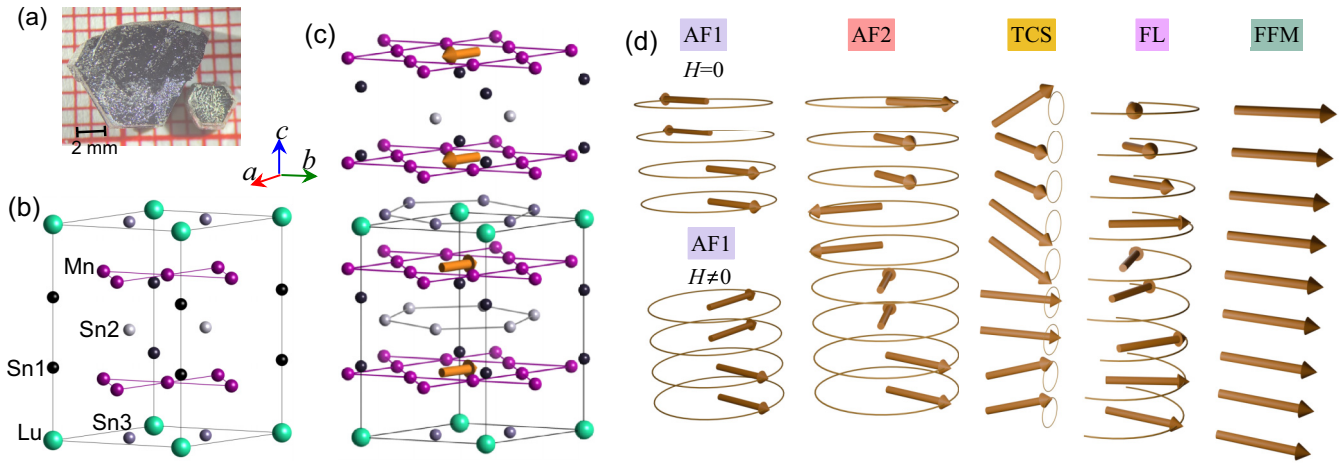

FIG. 2. (a) A picture of typical hexagonal prismatic $LuMn_6Sn_6$ crystals. (b) Sketch of $LuMn_6Sn_6$ structure generated with Vesta. The boxed area shows the primitive cell of the crystal structure. The three Sn positions are shown with three different shades of grey color. (c) Room temperature magnetic structures (AF1 phase) of $LuMn_6Sn_6$ at zero field based on the neutron diffraction measurements [34]. For simplicity, the magnetization of each manganese kagome sheet is shown by an arrow in the middle. (d) Sketch of different magnetic structures for YMn_6Sn_6 induced by a field applied along the a crystalline axis [23,36]. Arrows represent orientation of Mn moments within kagome sheets.

and the band topology depend on the R element type. Table I summarizes the lattice parameters and Néel temperatures in this family. The a and c lattice parameters of the Lu compound are in between the Sc and Y compound.

B. Magnetic properties

Zero field neutron scattering experiments on $LuMn_6Sn_6$ and YMn_6Sn_6 show that below the Néel temperature T_{N1}, a commensurate collinear AF structure forms first with the propagation vector $k = (0, 0, 1/2)$ [23,33,34,44]. This is the magnetic configuration of phase AF1, which is the dominant phase in the (H,T) phase diagram in Fig. 1. As the field increases in this phase, the moments gradually cant within the ab-plane, forming the coplanar canted AF1 state [22,23,44]. The magnetic structures of the AF1 phase with and without an applied field are schematically shown in Fig. 2(d). By cooling below T_{N2}, an incommensurate magnetic phase appears [23,33–35,44]. This phase has two nearly equal wave vectors and is known as a double-flat spiral or a double spiral. In this c-axis helical order, the Mn moments in each bilayer rotate by a nonconstant angle, requiring two distinct rotation angles to describe the directions of the moments [45]. For YMn_6Sn_6, the resulting complex arrangement with a nonuniform rotation of the moments leads to a supercell structure with $c' = 36c$ [34]. For $LuMn_6Sn_6$ this spiral phase corresponds to the AF2 phase as schematically shown in Fig. 2(d).

TABLE I. Lattice parameters and the Néel temperatures for RMn_6Sn_6, R = Sc, Y, Lu. T_{N1} marks the transition to a collinear antiferromagnetic state and T_{N2} is a transition to an incommensurate spiral state. $ScMn_6Sn_6$ lacks the collinear antiferromagnetic state.

R	a (Å)	c (Å)	T_{N1} (K)	T_{N2} (K)	References
Sc	5.4649	8.9608	390	–	[40]
	5.4692	8.9741	384	–	[35]
Lu	5.5076	8.9889	395	263	This study
	5.5079	8.9860	384	220–250	[35]
Y	5.541	9.035	345	–	[36]
	5.512	8.984	359	326	[43]
	5.5411	9.0228	340	333	[23]

Upon application of an external magnetic field in the ab plane, several field-induced magnetic phases rise. In YMn_6Sn_6 the magnetic phases identified are a transverse conical spiral (TCS), fan-shaped (FL), and forced ferromagnet (FFM) [23,36]. The cartoon in Fig. 2(d) schematically shows these phases. By comparing the (H, T) phase diagram in Fig. 1 with that of YMn_6Sn_6 [23,24], it can be inferred that $LuMn_6Sn_6$ likely adopts a TCS and a FL magnetic structure in phases III and IV, respectively.

Figure 3(a) presents the temperature, T, dependence of magnetization, M, obtained for a 0.05 T magnetic field applied along the a and c axes. The AF transition manifests itself as a kink in magnetization at $T_{N1} = 395$ K. A second transition, into an incommensurate spiral state, occurs at $T_{N2} = 263$ K, marking the boundary between the AF1 and AF2 magnetic phases. This latter transition appears more prominently as a drop in the $M(T)$ curve when the field is applied parallel to the a axis. The transitions temperatures are slightly higher than previously reported [35,46]. We observed that the use of higher purity tin and manganese results in a change of T_N's to slightly higher values. There is a slight difference between the T_N's values for the two orientations of the field. Our reported values are for measurements of M (T) in which the field is applied along the a axis. At 2 K, the measured magnetization was 188 emu/mole ($\sim$0.034 μ_B/f.u.) for 0.05 T field applied out-of-plane, which is comparable in magnitude to that of the sister compounds, YMn_6Sn_6 and $ScMn_6Sn_6$ [24,36,40].

The magnetic properties for the c-axis magnetic field are shown in Fig. S2 in the SM [42]. The magnetization curves for the field applied along the c axis show no field-induced transitions. This paper focuses on magnetotransport properties with an in-plane magnetic field.

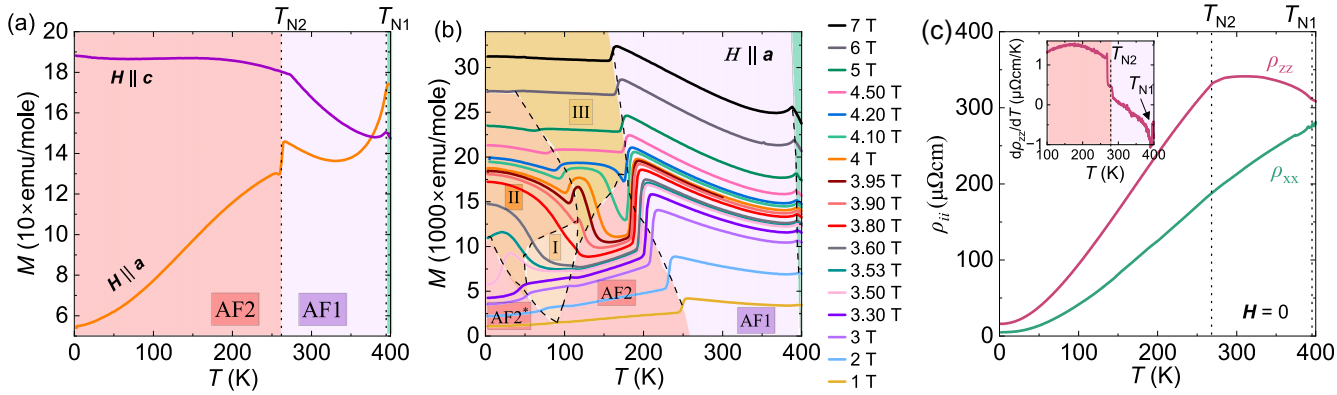

FIG. 3. (a) Magnetization M as a functions of temperature T for magnetic field $\mu_0 H = 0.05$ T applied parallel to the a and c axes of the $LuMn_6Sn_6$ crystal, obtained on heating the sample after zero-field-cooling (ZFC) down to ∼2 K. (b) $M(T)$ curves measured under several different magnetic field values for $\mu_0 H$ applied along the a axis. Dashed lines define the boundaries between different field-induced magnetic phases. (c) Electrical resistivity as a function of temperature, with the electric current applied along the a axis (ρ_{xx}) and c axis (ρ_{zz}) of the crystal. Inset shows the temperature derivative of ρ_{zz} in the vicinity of T_{N1} and T_{N2}. Dotted lines in panels (a, c) show antiferromagnetic transitions happening at T_{N1} and T_{N2}.

When larger a-axis fields are applied, $LuMn_6Sn_6$ exhibits rich magnetism at low temperatures. Upon cooling below 200 K, it undergoes a series of magnetic phase transitions, as shown by the strong field dependence of M in phases AF2*, I, II, and III in Fig. 3(b). Phase I was not clearly distinguishable in the field-dependence measurements of magnetization. Neutron scattering measurements by Do *et al.* [22] show a continued change in the ordering wave vector below 250 K and a distinct kink at 100 K. Therefore, we labeled the magnetic phase below 100 K by AF2* to communicate this discontinuity in the character of the wave vector.

The AF1 state in YMn_6Sn_6 [43,47] exists in a very narrow temperature range, as can be seen from the small temperature difference between T_{N1} and T_{N2} in Table I. This phase is absent in $ScMn_6Sn_6$ [40] which has a DS structure throughout the temperature range below its Néel temperature. However in $LuMn_6Sn_6$ the AF1 phase is much more extended in the phase diagram (Fig. 1). Direct comparison of the magnetic phase diagrams of $LuMn_6Sn_6$, YMn_6Sn_6 [23,24], and $ScMn_6Sn_6$ [38], reveals that the DS phase is divided into phases of I, II, AF2, and AF2* in the Lu compound. This is manifested in Fig. 3(b) by the strong response of the helical AF2 state to the magnetic field at lower temperatures. The temperature derivative of the $M(T)$ isotherm curves was used to construct the phase diagram, as shown by the square-shaped data points in Fig. 1.

C. Electrical transport properties

The intricate transport properties shown in Fig. 4 reveal several magnetic phases that are induced by the application of $\boldsymbol{H} \parallel \mathbf{a}$. The field derivatives of these curves were used in constructing the (H, T) phase diagram in Fig. 1 (detailed in Fig. S3 in the SM [42]).

The $M(H)$ isotherms in Fig. 4(a) resemble those of RMn_6Sn_6 (R= Sc and Y), albeit with the common magnetic phases appearing at much larger fields [24,36,38,48]. The abrupt change of M around 4 T in Fig. 4(a) (at AF2 to III phase boundary) suggests a first-order metamagnetic transition, which was seen in $ScMn_6Sn_6$ and YMn_6Sn_6 as well [36–38]. At low temperatures M starts to saturate at $\mu_0 H >$ 25 T, while for $ScMn_6Sn_6$ and YMn_6Sn_6 the FFM phase appears at $\mu_0 H >$ 3 T and 10 T, respectively [24,36–38,48]. The larger saturation field in $LuMn_6Sn_6$ indicates a stronger AF interaction between layers compared to the other sister compounds. The T dependence of the longitudinal resistivity in-plane (ρ_{xx}) and out-of-plane (ρ_{zz}) are shown in Fig. 3(c). The electric current was applied along the crystallographic a axis (c axis) to measure ρ_{xx} (ρ_{zz}). In Figs. 4(b)–4(e), the subscript i in ρ_{ji}, indicates the direction of the applied current and j denotes the direction of the measured voltage. A schematic of this measurement configuration is shown in Fig. 4(f).

The transition temperatures appear as steps and more clearly in the temperature derivative of ρ_{zz}, Fig. 3(c) inset. $\rho_{zz}(T)$ shows a negative concavity in T regions between T_{N1} and T_{N2}. Often, the resistivity of an itinerant antiferromagnet shows positive concavity as a function of temperature in its ordered state. This type of increase in electrical resistivity at the magnetic ordering temperature is commonly attributed to the formation of a superzone gap on the Fermi surface, where portions of the Fermi surface vanish, leading to an increase in resistivity [49]. This is a result of the Fermi surface reconstruction caused by the emergence of a new magnetic Brillouin zone, which gaps out certain regions of the Fermi surface. The increase in $\rho_{zz}(T)$ upon lowering the temperature between T_{N1} and T_{N2} could also be a result of incoherent interlayer transport, perhaps due to spin scattering.

Figure 3(c) shows that by further cooling below T_{N2}, ρ_{zz} shows a positive concavity, observed in the whole T range for ρ_{xx}, possibly due to the suppression of spin-disorder scattering. We obtained residual resistivity ratios $RRR = R_{300K}/R_{2K} = 22 - 44$ and a residual resistivity of $RR = 4 - 15$ μΩcm in different crystals.

Figures 4(c) and 4(d) show that both longitudinal resistivities increase parabolically with H in the AF2 phase and linearly in phase III. In the AF1 phase ρ_{zz} exhibit negative magnetoresistivity and ρ_{yy} shows smaller changes. Hall resistivity, shown in Fig. 4(b), appears to be more sensitive to phase transitions around AF1 and III than magnetization, showing

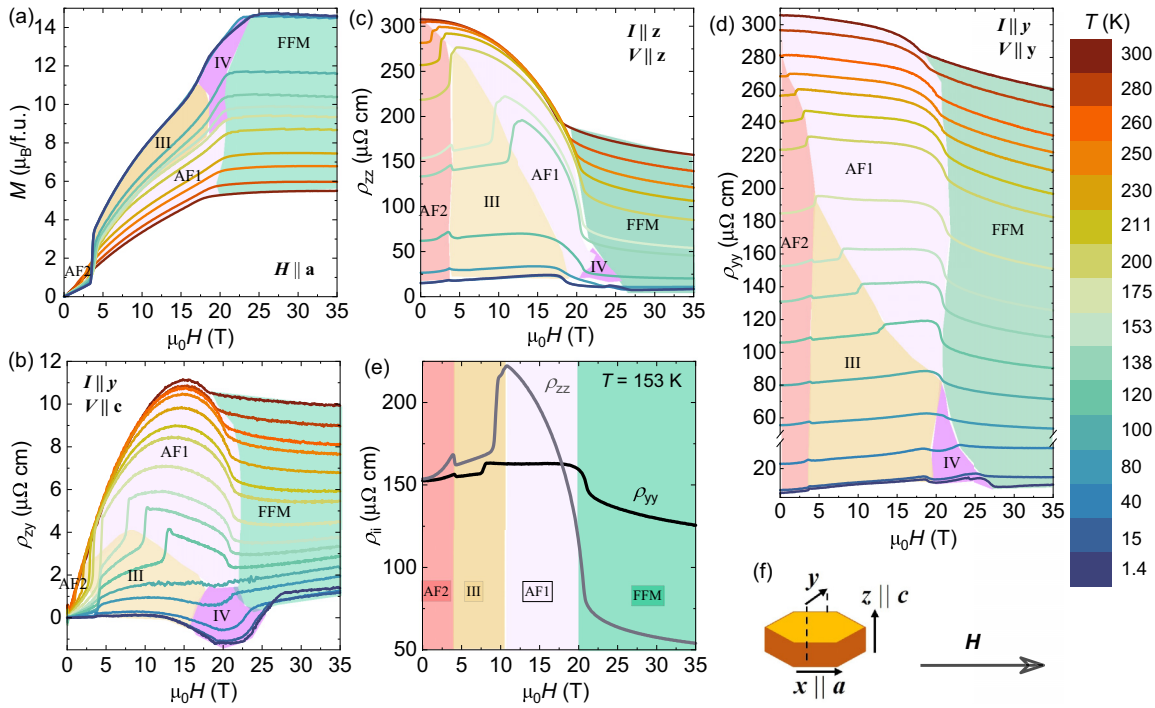

FIG. 4. Magnetotransport properties of $LuMn_6Sn_6$ for the magnetic field applied along the a axis. (a) magnetization M, (b) Hall resistivity ρ_{zy}, (c) longitudinal resistivity ρ_{zz}, and (d) longitudinal resistivity ρ_{yy} as a function of magnetic field at various temperatures. (e) Magnetoresistivities ρ_{yy} and ρ_{zz} show a strong anisotropy in the AF1 phase. The cartoon in (f) shows the directions of the applied electrical current, magnetic field, and the measured voltage. The different magnetic phases are colored and labeled according to Fig. 1.

a sudden increase, as the magnetic structure evolves. These sharp increases in ρ_{zy} are more pronounced at 120 K, 138 K, and 153 K and were consistently observed in multiple crystals and multiple batches.

At low fields, the field dependence of the Hall data have a positive slope, indicating that holes are the dominant charge carriers. We have obtained a rough estimate for the densities n and mobilities μ of the holes by fitting $\rho_{zy}(H)$ to a simple band Drude model, which are shown in Fig. S4 in the SM [42]. At room temperature, we obtained $n_{300K} = 5.5 \times 10^{18}$ cm^{-3} and $\mu_{300K} = 3721$ cm^{2}V^{-1}S^{-1}, which drop to smaller values at lower temperatures. We *estimate* the carrier concentration and mobility in the low-field regime, where the band splitting and magnetization effects are minimal. We also observed distinct Shubnikov-de Haas (SdH) oscillations in ρ_{zz} at 1.4 K in the FFM phase for $\mu_0 H > 27$ T with the field aligned along the a axis. The SdH oscillations are shown in Fig. S5 in the SM [42]. The analysis of the SdH signal, as explained in the SM [42], revealed a Fermi surface pocket with a k-space area of $A_k = 7.2$ nm^{-2}.

1. Anomalous Hall effect in the canted AF1 and FFM phases

We further explore the Hall effect data by examining the conductivity σ_{zz} and Hall conductivity σ_{zy}, shown in Fig. 5. These curves were obtained by inverting the resistivity tensor [50], following Eq. (1):

$$\begin{bmatrix} \sigma_{yy} & \sigma_{yz} \\ \sigma_{zy} & \sigma_{zz} \end{bmatrix} = \begin{bmatrix} \rho_{yy} & \rho_{yz} \\ \rho_{zy} & \rho_{zz} \end{bmatrix}^{-1} = \frac{1}{\rho_{yy}\rho_{zz} + \rho_{zy}^2} \begin{bmatrix} \rho_{zz} & -\rho_{yz} \\ -\rho_{zy} & \rho_{yy} \end{bmatrix}. \quad (1)$$

As Fig. 5(a) shows, there is a sudden increase in the Hall conductivity at field values where the metamagnetic transitions in the magnetization [Fig. 4(a)] occur. This happens at the boundary between the AF2 and AF1 phases. At these field strengths, the canting of magnetic moments along the applied field introduces an effective ferromagnetic component, which gives rise to an anomalous contribution to the Hall conductivity [see the schematics for the canting of the moments in Fig. 2(d)]. Note that canting of the magnetic moments happens in the plane [22,23,44]. The anomalous Hall conductivity (AHC) in the AF1 phase, σ_{zy}^A, is estimated directly from the sharp increase in σ_{zy} values marked by the black vertical lines in Fig. 5(a). These values are plotted in the inset of Fig. 5(a) along with the conductivity values.

The intrinsic AHE, which is related to the Berry curvatures in momentum space theoretically should be less than e^2/ha [1,6]. Here, e is the elementary charge, h is Planck's constant, and a is the typical lattice parameter, which for $LuMn_6Sn_6$ would be ≈800 S cm^{-1}. The extracted σ_{zy}^A values in the inset of Fig. 5(a) are within the limit of the intrinsic AHC. Therefore, we conclude that the sudden increase in the ρ_{zy} values upon entering phase AF1 is due to intrinsic contributions to the AHE. The maximum value of σ_{zy}^A that we can unambiguously extract is about 70 S cm^{-1} at 175 K. This is less than the typical values for intrinsic AHC in ferromagnets such as Fe (>1000 S cm^{-1}) [51] or in itinerant d-electron AF materials such as Mn_3Sn, Mn_3Ge, and NbMnP (100–450 S cm^{-1}) [4,5,7].

Another possible explanation for the sudden increase in the Hall effect data is the metamagnetic multiband Hall effect [52]. In this scenario, the nonmonotonic character of

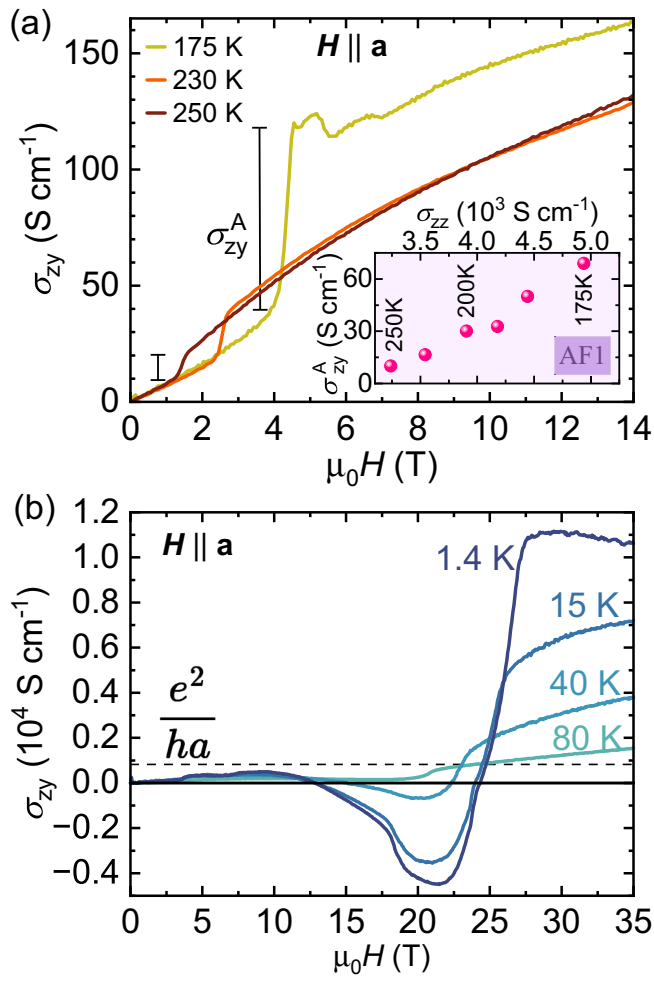

FIG. 5. Hall conductivity in $LuMn_6Sn_6$ as a function of magnetic field oriented along the a axis at high temperatures in the canted AF1 phase (a) and low temperatures (b). The vertical lines in panel (a) show the extracted anomalous contribution σ^A_{zy} to the Hall conductivity in the canted AF1 phase, which are plotted against conductivity in the inset. The upper threshold value of the intrinsic AHC in three-dimensions (e^2/ha) is indicated by the dashed line in panel (b).

the Hall effect is attributed to a band-dependent mobility modulation resulting from 4*f*-5*d* interactions. The Kondo-like Hamiltonian in this model is particularly effective at low temperatures and low fields, while the sharp jump in ρ_{zy} in $LuMn_6Sn_6$ occurs at high fields and relatively elevated temperatures. Therefore, we conclude that the sharp increase in the Hall conductivity at the border of the AF2 to AF1 phase is related to the formation of a ferromagnetic component as the result of canting of the moments.

We now turn our attention to the low-temperature transport properties. Scaling relations between longitudinal and Hall conductivities are often employed empirically to identify the dominant scattering mechanisms that contribute to anomalous transport [1]. The moderate longitudinal conductivity of $\sigma_{zz}(T = 1.4\ \text{K})$ in the order of 10^5 S cm^{-1} places $LuMn_6Sn_6$ in the moderate conductivity regime where intrinsic scattering phenomena dominate the AHE. However, the σ_{zy} values increase sharply at low T's when the field is ramped into the FFM phase, as shown in Fig. 5(b). In fact, Hall conductivity at 1.4 K reaches 11 000 S cm^{-1}, exceeding the intrinsic quantized AHE of e^2/ha by two orders of magnitude. This shows a clear deviation from the conventional scaling relations established for ferromagnets. Such large AHE with electron-scattering origin (extrinsic mechanisms–such as skew scattering) has been reported in the chiral ferromagnetic state of MnGe thin films [6].

Equally interesting is the sudden change in the sign of σ_{zy} near 25 T, at the boundary of phase IV(V) to FFM phase. Below 25 T, the Hall conductivity is dominated by electron bands. However, once the field exceeds 25 T, σ_{zy} becomes positive, indicating a shift in dominant charge carriers from electrons to holes. By directly comparing the magnetic phase diagram of $LuMn_6Sn_6$ (Fig. 1) with YMn_6Sn_6 [23,24], it can be inferred that the magnetic structure undergoes a transition from a fan-like (FL) phase to the FFM phase around 25 T. The observed sign change in σ_{zy} may be related to a magnetic field-induced reconstruction of the Fermi surface. In particular, a magnetization-driven Lifshitz transition has been reported for YMn_6Sn_6 [24], suggesting a similar mechanism could be operative in $LuMn_6Sn_6$. Our results suggest the need for further theoretical studies on the electronic band structure of $LuMn_6Sn_6$, the enhancement of Berry curvature, and its relationship to the observed AHE at these field-induced magnetic phases.

2. Pitfalls in the extraction of THE and the role of resistivity anisotropy

In this section, we demonstrate the limitations of standard methods used to extract the topological Hall effect (THE). To do so, we first apply these empirical techniques to the AF1 phase, which is not expected to exhibit any THE. This allows us to assess which method yields results most consistent with theoretical expectations. In the following section, we then apply the method that shows the best agreement to phase III (the TCS phase), which is reported to show a THE in related compounds such as YMn_6Sn_6 [36,37] and $ErMn_6Sn_6$ [28].

The Hall effect behavior in Fig. 4(b) is quite intriguing. At high temperatures, ρ_{zy} shows a hump within the AF1 phase that could mistakenly be regarded as resulting from a THE contribution. The three main contributions to the Hall effect are the ordinary Hall effect ρ^O_{zy}, the anomalous Hall resistivity ρ^A_{zy}, and the topological Hall resistivity ρ^T_{zy}; $\rho_{zy} = \rho^O_{zy} + \rho^A_{zy} + \rho^T_{zy}$. The THE is extracted by first fitting the high field Hall data–where only the ordinary and anomalous Hall effects are present–to isolate their contributions. This fitted background is then subtracted from the total Hall signal, and the remaining part is attributed to the topological Hall effect. The process of extracting the topological Hall resistivity is detailed in Sec. S 6 of the SM [42] for a representative temperature of 40 K.

The ordinary Hall effect is approximately linear with respect to the applied field, $\rho^O_{zy} = R_0 B$ [50]. Where, R_0 is the ordinary Hall coefficient and B is the induction field. In a multi-band system, R_0 can be field dependent. As shown in Refs. [43,53], the electronic band structure of $LuMn_6Sn_6$ and

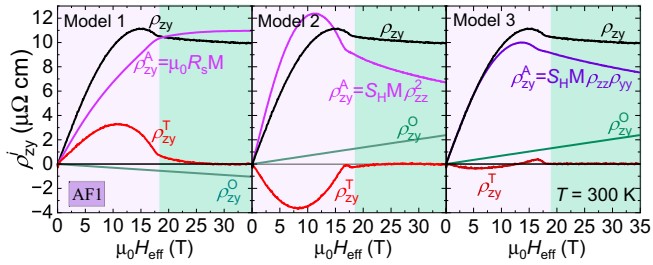

FIG. 6. Comparison of empirical approaches for modeling the AHE in the extraction of the THE. Panels display the field dependence of Hall resistivity ρ_{zy} and its components: ordinary (ρ^O_{zy}), anomalous (ρ^A_{zy}), and topological (ρ^T_{zy}) for $LuMn_6Sn_6$ at 300 K. ρ^A_{zy} is estimated using three empirical models. In model 1, ρ^A_{zy} is assumed to be linearly proportional to the magnetization. In models 2 and 3, ρ^A_{zy} is taken to be proportional to the magnetization multiplied by the square of the longitudinal resistivity. Model 2 assumes isotropic longitudinal resistivity setting $\rho_{yy} = \rho_{zz}$, leading to an exaggerated value for ρ^T_{zy}. In model 3, ρ^A_{zy} is derived by accounting for the anisotropy in the longitudinal resistivity. Note that $\chi_{ijk} = 0$ for the AF1 phase, so no THE is expected.

YMn_6Sn_6 are quite complex, and therefore the multiband effects are likely to play significant role.

Two empirical equations are frequently employed in the experimental analysis of the AHE [28,36–38,54]. One of them, derived for ferromagnets, is given by $\rho^A_{zy} = \mu_0 R_s M$, where μ_0 is the vacuum permeability and R_s is the anomalous Hall coefficient. This relation for ρ^A_{zy} is used in model 1 in Fig. 6 for the extraction of ρ^T_{zy}. Using this empirical relation for the AHE results in an apparent topological Hall resistivity that peaks at 3 μΩ cm at 300 K.

Another commonly used relation is expressed as $\rho^A_{zy} = R_s M \rho_{zz}\rho_{yy}$, where $\rho_{zz}(\rho_{yy})$ and ρ_{zy} correspond to longitudinal and Hall resistivities, respectively. Here, ρ^A_{zy} is derived using Eq. (1) and assuming that anomalous Hall conductivity is proportional to magnetization. We refer to this equation for the AHE as model 3.

In most metallic systems, longitudinal resistivities are isotropic, making it reasonable to express $\rho^A_{zy} = R_s M \rho^2_{yy}$. However, in noncubic compounds with anisotropic resistivity, especially in out-of-plane measurements (zy plane), if both longitudinal resistivities are not carefully considered, as shown in Fig. 6 by model 2, the resulting AHE is overestimated. This overestimation of ρ^A_{zy} consequently leads to an exaggerated value of 4 μΩ cm for ρ^T_{zy}, which is larger than the values reported for well-established skyrmionic systems such as MnSi [11] and Gd_2PdSi_3 [14].

Why does accounting for the anisotropy of magnetoresistance make such a big difference in $LuMn_6Sn_6$? As shown in Figs. 4(c) and 4(d), in the canted AF1 phase, ρ_{zz} exhibits a strong negative magnetoresistivity, while ρ_{yy} curves remain relatively flat. The strong anisotropy in the longitudinal resistivities in the AF1 phase is depicted in Fig. 4(e) for a representative temperature of 153 K. This pronounced anisotropy in the magnetoresistivities plays a critical role in the proper analysis of the Hall effect data. This can be seen by comparing panels in model 2 and model 3 in Fig. 6. In model 3, we have now included the anisotropy in the magnetoresistivity, however, we still obtain a nonzero topological Hall effect at 300 K, where the magnetic structure is coplanar canted antiferromagnet with zero scalar spin chirality–conditions under which a THE is not expected.

As demonstrated in this section (and also in the next one), there are limitations in using these experimental tools to analyze the contribution from the AHE. Attention must also be paid to the procedure for separating the contribution from the ordinary Hall effect. In systems where there is a possibility of a change in the Fermi surface at different magnetic structures such as Lifschitz transitions [24], R_0 is no longer a constant, and the contribution from the ordinary Hall effect cannot be assumed to be equal in all magnetic phases. At minimum, we recommend using model 3 to estimate THE to approximately estimate the anomalous Hall contribution in anisotropic phases. The need for a more thorough consideration in identifying emergent magnetic fields in frustrated itinerant magnets has recently been discussed by Refs. [52,55] as well.

3. Topological Hall Effect in phase III (transverse conical spiral, TCS)

We now turn our attention to the magnetic phase III and the possibility of observing the THE in this phase. THE is a hallmark of scalar spin chirality, and is observed in skyrmionic lattices such as MnSi [11], FeGe [56], Gd_2PdSi_3 [14], and $EuAl_4$ [57]. To the best of our knowledge, no magnetic phase in $LuMn_6Sn_6$ has been identified to host a nonzero scalar spin chirality.

By directly comparing the magnetic phase diagrams of $LuMn_6Sn_6$ and YMn_6Sn_6 [23,24] along with neutron scattering studies reported in Ref. [22], it can be concluded that the magnetic structure of this phase is a transverse conical spiral (TCS). A THE is not expected in this phase due to its zero scalar spin chirality [23,36]. However, the TCS phase in YMn_6Sn_6 has been reported to exhibit a THE [36,37]. The THE occurs at high temperatures, leading to the proposal of a dynamical mechanism as a possible explanation for the appearance of THE in the TCS phase, despite the absence of scalar spin chirality. It has been suggested that magnon fluctuations, coupled with the strongly two-dimensional nature of the magnetic exchange, may explain the observed THE in YMn_6Sn_6 [36]. Following this observation, we examine the THE in the TCS phase of $LuMn_6Sn_6$.

The derived topological contribution to the Hall resistivity at 40, 80, and 153 K are plotted as a function of effective magnetic field in Fig. 7 (see Fig. S6 in the SM [42] for detailed calculations for a representative temperature of 40 K). We were unable to clearly separate the contributions of ρ^A_{zy} and ρ^T_{zy} to ρ_{zy} at temperatures below 40 K. In our analysis, for the AHE we used the empirical relation from model 3, $\rho^A_{zy} = R_s M \rho_{zz}\rho_{yy}$, as it provided slightly better agreement with the expected absence of a THE in the AF1 phase (Sec. III C 2).

After properly accounting for the anisotropy of the longitudinal resistivity, we obtained a maximum value of 0.93 μΩ cm at 40 K for ρ^T_{zy} in phase III (the TCS phase). This is within the reported value of 1 μΩ cm for the TCS phase of YMn_6Sn_6 and $ScMn_6Sn_6$ at 245 K [36–38]. We note that the value of THE would be significantly larger if we had used model 2

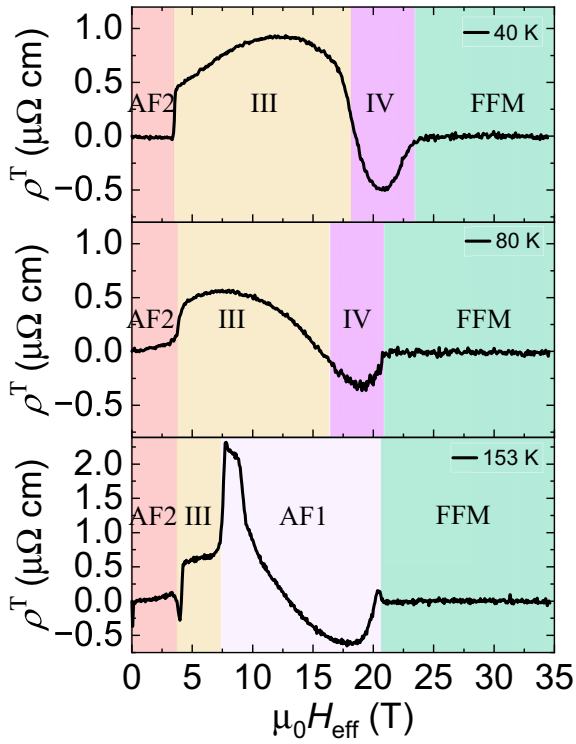

FIG. 7. Extracted topological Hall ρ^T at several constant temperatures. The anomaly in ρ^T across the border of phase III and AF1 at 153 K, is a result of an artifact due to mismatch between the transition fields in ρ_{yy} and ρ_{zz}. This mismatch can be see in Fig. 4(e) around 10 T. The observation of THE at phase AF1 with $\chi_{ijk} = 0$ calls into question our standard methods for extracting the THE.

for the estimation of the AHE (as we have emphasized in Sec. III C 2).

ρ_{zy}^T in phase III exhibits slightly lower values at elevated temperatures of 80 and 153 K. A nonvanishing THE is also observed in phase IV, which is most likely associated with a FL magnetic structure [22]. Particularly striking is the presence of a nonzero THE at 153 K in the AF1 phase. Given that AF1 is characterized by a canted antiferromagnetic structure with no scalar spin chirality, this observation is unexpected. It is concerning that THE is present in all three phases—III, AF1, and IV—with nearly comparable magnitudes. Notably, the THE in phase III is exceptionally robust, persisting across a wide magnetic field range of up to 20 T.

The observations in this section and Sec. III C 2 raise questions about the reliability of our conventional methods for extracting THE. Our observations cast doubt on whether the TCS phase truly exhibits a topological Hall signal. As discussed in Sec. III C 2, there are limitations in using the empirical relations for partitioning the Hall effect data when interpreting topological transport data. The peculiar behavior of THE in RMn_6Sn_6 suggests the need for further theoretical studies to understand the origin of the emerging THE and AHE, and more thorough consideration when dealing with anomalies in the Hall effect data.

IV. CONCLUSION

Our detailed magnetotransport study of the metallic kagome compound $LuMn_6Sn_6$ reveals a rich magnetic phase diagram driven by competing interactions under an applied in-plane magnetic field. Our investigation of the Hall effect in the canted antiferromagnetic (AF1) state, shows an anomalous Hall effect (AHE) which we attribute to intrinsic contributions. We measured a Hall conductivity of 11 000 Scm^{-1} at 1.4 K, which exceeds the intrinsic quantized AHE of e^2/ha by two orders of magnitude, despite moderate longitudinal conductivity σ_{zz} on the order of 10^5 S cm^{-1}.

We also demonstrate the limitations of standard methods used to estimate the various contributions to the Hall effect. These limitations can give rise to a large apparent topological Hall effect (THE) in coplanar magnetic phases where a true topological Hall response is not anticipated. This issue is exacerbated when the anisotropy in the longitudinal resistivity is not adequately accounted for. Furthermore, even when resistivity anisotropy is considered, a residual THE-like signal persists in phases III, IV, and AF1, despite their lack of scalar spin chirality. These findings highlight the need for more rigorous theoretical frameworks to accurately interpret the Hall effect data in complex magnetic compounds.

ACKNOWLEDGMENTS

S.M., R.P.M., W.R.M., and D.G.M. acknowledge the support from the Gordon and Betty Moore Foundation's EPiQS initiative, Grant No. GBMF9069 and the support from AFOSR MURI Grant No. FA9550-20-1-0322. This publication is funded in part by a QuantEmX grant from ICAM and the Gordon and Betty Moore Foundation through Grant No. GBMF9616 to S.M. L.B. is supported by the U.S. Department of Energy (DOE) through the BES program, Award No. DE-SC0002613. X-ray diffraction was performed at the Institute for Advanced Materials & Manufacturing (IAMM) Diffraction facility, located at the University of Tennessee, Knoxville. The National High Magnetic Field Laboratory is supported by the National Science Foundation through Grants No. NSF/DMR-1644779 and No. NSF/DMR-2128556 and the State of Florida.

DATA AVAILABILITY

The data that support the findings of this article are available from the authors upon request.

[1] N. Nagaosa, J. Sinova, S. Onoda, A. H. MacDonald, and N. P. Ong, Anomalous Hall effect, Rev. Mod. Phys. **82**, 1539 (2010).

[2] L. Šmejkal, A. H. MacDonald, J. Sinova, S. Nakatsuji, and T. Jungwirth, Anomalous Hall antiferromagnets, Nat. Rev. Mater. **7**, 482 (2022).

[3] Y. Machida, S. Nakatsuji, S. Onoda, T. Tayama, and T. Sakakibara, Time-reversal symmetry breaking and spontaneous Hall effect without magnetic dipole order, Nature (London) **463**, 210 (2010).

[4] S. Nakatsuji, N. Kiyohara, and T. Higo, Large anomalous Hall effect in a non-collinear antiferromagnet at room temperature, Nature (London) **527**, 212 (2015).

[5] N. Kiyohara, T. Tomita, and S. Nakatsuji, Giant anomalous Hall effect in the chiral antiferromagnet Mn_3Ge, Phys. Rev. Appl. **5**, 064009 (2016).

[6] Y. Fujishiro, N. Kanazawa, R. Kurihara, H. Ishizuka, T. Hori, F. S. Yasin, X. Yu, A. Tsukazaki, M. Ichikawa, M. Kawasaki *et al.*, Giant anomalous Hall effect from spin-chirality scattering in a chiral magnet, Nat. Commun. **12**, 317 (2021).

[7] Y. Arai, J. Hayashi, K. Takeda, H. Tou, H. Sugawara, and H. Kotegawa, Intrinsic anomalous Hall effect arising from antiferromagnetism as revealed by high-quality NbMnP, J. Phys. Soc. Jpn. **93**, 063702 (2024).

[8] H. Kotegawa, H. Tanaka, Y. Takeuchi, H. Tou, H. Sugawara, J. Hayashi, and K. Takeda, Large anomalous Hall conductivity derived from an f-electron collinear antiferromagnetic structure, Phys. Rev. Lett. **133**, 106301 (2024).

[9] L. Šmejkal, J. Sinova, and T. Jungwirth, Beyond conventional ferromagnetism and antiferromagnetism: A phase with nonrelativistic spin and crystal rotation symmetry, Phys. Rev. X **12**, 031042 (2022).

[10] P. Bruno, V. K. Dugaev, and M. Taillefumier, Topological Hall effect and Berry phase in magnetic nanostructures, Phys. Rev. Lett. **93**, 096806 (2004).

[11] A. Neubauer, C. Pfleiderer, B. Binz, A. Rosch, R. Ritz, P. G. Niklowitz, and P. Böni, Topological Hall effect in the A phase of MnSi, Phys. Rev. Lett. **102**, 186602 (2009).

[12] B. Binz and A. Vishwanath, Chirality induced anomalous-Hall effect in helical spin crystals, Phys. B: Condens. Matter **403**, 1336 (2008).

[13] N. Kanazawa, Y. Onose, T. Arima, D. Okuyama, K. Ohoyama, S. Wakimoto, K. Kakurai, S. Ishiwata, and Y. Tokura, Large topological Hall effect in a short-period helimagnet MnGe, Phys. Rev. Lett. **106**, 156603 (2011).

[14] T. Kurumaji, T. Nakajima, M. Hirschberger, A. Kikkawa, Y. Yamasaki, H. Sagayama, H. Nakao, Y. Taguchi, T.-h. Arima, and Y. Tokura, Skyrmion lattice with a giant topological Hall effect in a frustrated triangular-lattice magnet, Science **365**, 914 (2019).

[15] T. Kida, L. Fenner, A. Dee, I. Terasaki, M. Hagiwara, and A. Wills, The giant anomalous Hall effect in the ferromagnet Fe_3Sn_2—a frustrated kagome metal, J. Phys.: Condens. Matter **23**, 112205 (2011).

[16] Q. Wang, S. Sun, X. Zhang, F. Pang, and H. Lei, Anomalous Hall effect in a ferromagnetic Fe_3Sn_2 single crystal with a geometrically frustrated Fe bilayer kagome lattice, Phys. Rev. B **94**, 075135 (2016).

[17] B. P. Belbase, L. Ye, B. Karki, J. I. Facio, J.-S. You, J. G. Checkelsky, J. van den Brink, and M. P. Ghimire, Large anomalous Hall effect in single crystals of the kagome Weyl ferromagnet Fe_3Sn, Phys. Rev. B **108**, 075164 (2023).

[18] M. Ikhlas, T. Tomita, T. Koretsune, M.-T. Suzuki, D. Nishio-Hamane, R. Arita, Y. Otani, and S. Nakatsuji, Large anomalous Nernst effect at room temperature in a chiral antiferromagnet, Nat. Phys. **13**, 1085 (2017).

[19] Y. Zhang, Y. Sun, H. Yang, J. Železný, S. P. P. Parkin, C. Felser, and B. Yan, Strong anisotropic anomalous Hall effect and spin Hall effect in the chiral antiferromagnetic compounds Mn_3X (X = Ge, Sn, Ga, Ir, Rh, and Pt), Phys. Rev. B **95**, 075128 (2017).

[20] Q. Wang, Y. Xu, R. Lou, Z. Liu, M. Li, Y. Huang, D. Shen, H. Weng, S. Wang, and H. Lei, Large intrinsic anomalous Hall effect in half-metallic ferromagnet $Co_3Sn_2S_2$ with magnetic Weyl fermions, Nat. Commun. **9**, 3681 (2018).

[21] X. Xu, J.-X. Yin, Z. Qu, and S. Jia, Quantum interactions in topological R166 kagome magnet, Rep. Prog. Phys. **86**, 114502 (2023).

[22] S.-H. D. *et al.*, (unpublished).

[23] R. L. Dally, J. Lynn, N. J. Ghimire, D. Michel, P. Siegfried, and I. I. Mazin, Chiral properties of the zero-field spiral state and field-induced magnetic phases of the itinerant kagome metal YMn_6Sn_6, Phys. Rev. B **103**, 094413 (2021).

[24] P. E. Siegfried, H. Bhandari, D. C. Jones, M. P. Ghimire, R. L. Dally, L. Poudel, M. Bleuel, J. W. Lynn, I. I. Mazin, and N. J. Ghimire, Magnetization-driven Lifshitz transition and charge-spin coupling in the kagome metal YMn_6Sn_6, Commun. Phys. **5**, 58 (2022).

[25] Y. Lee, R. Skomski, X. Wang, P. P. Orth, Y. Ren, B. Kang, A. K. Pathak, A. Kutepov, B. N. Harmon, R. J. McQueeney, I. I. Mazin, and L. Ke, Interplay between magnetism and band topology in the kagome magnets RMn_6Sn_6, Phys. Rev. B **108**, 045132 (2023).

[26] D. C. Jones, S. Das, H. Bhandari, X. Liu, P. Siegfried, M. P. Ghimire, S. S. Tsirkin, I. I. Mazin, and N. J. Ghimire, Origin of spin reorientation and intrinsic anomalous Hall effect in the kagome ferrimagnet $TbMn_6Sn_6$, Phys. Rev. B **110**, 115134 (2024).

[27] S. T. Yazdi, N. Tajabor, M. R. Roknabadi, M. Behdani, and F. Pourarian, Magnetoelastic properties of $ErMn_6Sn_6$ intermetallic compound, J. Magn. Magn. Mater. **324**, 723 (2012).

[28] K. Fruhling, A. Streeter, S. Mardanya, X. Wang, P. Baral, O. Zaharko, I. I. Mazin, S. Chowdhury, W. D. Ratcliff, and F. Tafti, Topological Hall effect induced by chiral fluctuations in $ErMn_6Sn_6$, Phys. Rev. Mater. **8**, 094411 (2024).

[29] T. Asaba, S. M. Thomas, M. Curtis, J. D. Thompson, E. D. Bauer, and F. Ronning, Anomalous Hall effect in the kagome ferrimagnet $GdMn_6Sn_6$, Phys. Rev. B **101**, 174415 (2020).

[30] L. Gao, S. Shen, Q. Wang, W. Shi, Y. Zhao, C. Li, W. Cao, C. Pei, J.-Y. Ge, G. Li *et al.*, Anomalous Hall effect in ferrimagnetic metal RMn_6Sn_6 (R = Tb, Dy, Ho) with clean Mn kagome lattice, Appl. Phys. Lett. **119**, 092405 (2021).

[31] F. Kabir, R. Filippone, G. Dhakal, Y. Lee, N. Poudel, J. Casey, A. P. Sakhya, S. Regmi, R. Smith, P. Manfrinetti *et al.*, Unusual magnetic and transport properties in $HoMn_6Sn_6$ kagome magnet, Phys. Rev. Mater. **6**, 064404 (2022).

[32] Nil L, T. Victa Trevisan, and R. J. McQueeney, High-field magnetic phase diagrams of the RMn_6Sn_6 (R= Gd–Tm) kagome metals, Phys. Rev. B **111**, 054410 (2025).

[33] G. Venturini, R. Welter, B. Malaman, and E. Ressouche, Magnetic structure of YMn_6Ge_6 and room temperature magnetic structure of $LuMn_6Sn_6$ obtained from neutron diffraction study, J. Alloys Compd. **200**, 51 (1993).

[34] G. Venturini, D. Fruchart, and B. Malaman, Incommensurate magnetic structures of RMn_6Sn_6 (R = Sc, Y, Lu) compounds

from neutron diffraction study, J. Alloys Compd. **236**, 102 (1996).

[35] A. Matsuo, K. Suga, K. Kindo, L. Zhang, E. Brück, K. Buschow, F. De Boer, C. Lefèvre, and G. Venturini, Study of the Mn–Mn exchange interactions in single crystals of RMn$_6$Sn$_6$ compounds with R= Sc, Y, and Lu, J. Alloys Compd. **408**, 110 (2006).

[36] N. J. Ghimire, R. L. Dally, L. Poudel, D. Jones, D. Michel, N. T. Magar, M. Bleuel, M. A. McGuire, J. Jiang, J. Mitchell *et al.*, Competing magnetic phases and fluctuation-driven scalar spin chirality in the kagome metal YMn$_6$Sn$_6$, Sci. Adv. **6**, eabe2680 (2020).

[37] Q. Wang, K. J. Neubauer, C. Duan, Q. Yin, S. Fujitsu, H. Hosono, F. Ye, R. Zhang, S. Chi, K. Krycka, H. Lei, and P. Dai, Field-induced topological Hall effect and double-fan spin structure with a c-axis component in the metallic kagome antiferromagnetic compound YMn$_6$Sn$_6$, Phys. Rev. B **103**, 014416 (2021).

[38] H. Zhang, C. Liu, Y. Zhang, Z. Hou, X. Fu, X. Zhang, X. Gao, and J. Liu, Magnetic field-induced nontrivial spin chirality and large topological Hall effect in kagome magnet ScMn$_6$Sn$_6$, Appl. Phys. Lett. **121**, 202401 (2022).

[39] S. Roychowdhury, A. M. Ochs, S. N. Guin, K. Samanta, J. Noky, C. Shekhar, M. G. Vergniory, J. E. Goldberger, and C. Felser, Large room temperature anomalous transverse thermoelectric effect in kagome antiferromagnet YMn$_6$Sn$_6$, Adv. Mater. **34**, 2201350 (2022).

[40] R. P. Madhogaria, S. Mozaffari, H. Zhang, W. R. Meier, S.-H. Do, R. Xue, T. Matsuoka, and D. G. Mandrus, Topological Nernst and topological thermal Hall effect in rare-earth kagome ScMn$_6$Sn$_6$, Phys. Rev. B **108**, 125114 (2023).

[41] Y. Zhu, D. Zhang, G. Zheng, K.-W. Chen, H. Bhandari, K. Jenkins, A. Chan, N. J. Ghimire, and L. Li, Geometrical Nernst effect in the kagome magnet YMn$_6$Sn$_4$Ge$_2$, Phys. Rev. B **110**, 195125 (2024).

[42] See Supplemental Material at http://link.aps.org/supplemental/10.1103/hwz4-z9mm for x-ray diffraction analysis, magnetic susceptibility data for the field along the crystalline c-axis, details on building the phase diagram, charge carrier density and mobility, quantum oscillation, and estimation of the topological Hall resistivity.

[43] M. Li, Q. Wang, G. Wang, Z. Yuan, W. Song, R. Lou, Z. Liu, Y. Huang, Z. Liu, H. Lei, Z. Yin, and S. Wang, Dirac cone, flat band and saddle point in kagome magnet YMn$_6$Sn$_6$, Nat. Commun. **12**, 3129 (2021).

[44] H. Zhang, X. Feng, T. Heitmann, A. I. Kolesnikov, M. B. Stone, Y.-M. Lu, and X. Ke, Topological magnon bands in a room-temperature kagome magnet, Phys. Rev. B **101**, 100405(R) (2020).

[45] E. Rosenfeld and N. Mushnikov, Double-flat-spiral magnetic structures: Theory and application to the RMn$_6$Sn$_6$ compounds, Phys. B: Condens. Matter **403**, 1898 (2008).

[46] G. Venturini, B. C. El Idrissi, and B. Malaman, Magnetic properties of RMn$_6$Sn$_6$ (R= Sc, Y, Gd-Tm, Lu) compounds with HfFe$_6$Ge$_6$ type structure, J. Magn. Magn. Mater. **94**, 35 (1991).

[47] K. Uhlířová, V. Sechovský, F. de Boer, S. Yoshii, T. Yamamoto, M. Hagiwara, C. Lefèvre, and G. Venturini, Magnetic properties and Hall effect of single-crystalline YMn$_6$Sn$_6$, J. Magn. Magn. Mater. **310**, 1747 (2007).

[48] A. Kitaori, N. Kanazawa, T. Yokouchi, F. Kagawa, N. Nagaosa, and Y. Tokura, Emergent electromagnetic induction beyond room temperature, Proc. Natl. Acad. Sci. USA **118**, e2105422118 (2021).

[49] P. K. Das, N. Kumar, R. Kulkarni, S. Dhar, and A. Thamizhavel, Anisotropic magnetic properties and superzone gap formation in CeGe single crystal, J. Phys.: Condens. Matter **24**, 146003 (2012).

[50] C. Kittel, *Solid State Physics*, Vol. 3 (Shell Development Company, Emeryville, CA, 1955).

[51] T. Miyasato, N. Abe, T. Fujii, A. Asamitsu, S. Onoda, Y. Onose, N. Nagaosa, and Y. Tokura, Crossover behavior of the anomalous Hall effect and anomalous Nernst effect in itinerant ferromagnets, Phys. Rev. Lett. **99**, 086602 (2007).

[52] T. Kurumaji, S. Fang, L. Ye, S. Kitou, and J. G. Checkelsky, Metamagnetic multiband Hall effect in Ising antiferromagnet ErGa$_2$, Proc. Natl. Acad. Sci. USA **121**, e2318411121 (2024).

[53] M. Li, Q. Wang, L. Zhou, W. Song, H. Ma, P. Ding, A. Fedorov, Y. Huang, B. Büchner, H. Lei *et al.*, Visualizing the electronic structure of kagome magnet LuMn$_6$Sn$_6$ by angle-resolved photoemission spectroscopy, Chin. Phys. B **33**, 117101 (2024).

[54] Y. Gao, Q. Yin, Q. Wang, Z. Li, J. Cai, T. Zhao, H. Lei, S. Wang, Y. Zhang, and B. Shen, Spontaneous (anti)meron chains in the domain walls of van der Waals ferromagnetic $Fe_{5-x}GeTe_2$, Adv. Mater. **32**, 2005228 (2020).

[55] G. Kimbell, C. Kim, W. Wu, M. Cuoco, and J. W. Robinson, Challenges in identifying chiral spin textures via the topological Hall effect, Commun. Mater. **3**, 19 (2022).

[56] M. Leroux, M. J. Stolt, S. Jin, D. V. Pete, C. Reichhardt, and B. Maiorov, Skyrmion lattice topological Hall effect near room temperature, Sci. Rep. **8**, 15510 (2018).

[57] R. Takagi, N. Matsuyama, V. Ukleev, L. Yu, J. S. White, S. Francoual, J. R. Mardegan, S. Hayami, H. Saito, K. Kaneko *et al.*, Square and rhombic lattices of magnetic skyrmions in a centrosymmetric binary compound, Nat. Commun. **13**, 1472 (2022).